Interface Engineering to Eliminate Hysteresis of Carbon-based Planar Heterojunction Perovskite Solar Cells via CuSCN Incorporation

*Yang Yang[a], Ngoc Duy Pham[a], Disheng Yao[a], Lijuan Fan[b], Minh Tam Hoang[a], Vincent Tiing Tiong[a], Zhaoxiang Wang[b], Huaiyong Zhu[a], Hongxia Wang[a,] **

[a]School of Chemistry, Physics and Mechanical Engineering, Science and Engineering Faculty, Queensland University of Technology, Brisbane 4001, Australia

[b]Key Laboratory for Renewable Energy, Institute of Physics, Chinese Academy of Sciences, P. O. Box 603, Beijing 100190, China

*Corresponding Author.

E-mail address: hx.wang@qut.edu.au (H. Wang).

ABSTRACT

Carbon electrode with low cost and high stability has exhibited competitiveness for its practical application in organic-inorganic hybrid perovskite solar cells. Nonetheless, issues such as poor interface contact with adjacent perovskite layer and obvious hysteresis phenomenon are bottlenecks that need to be overcome to make carbon based PSCs (C-PSCs) more attractive in practice. Herein, we report an effective method to enhance the interfacial charge transport of C-PSCs by introducing CuSCN material into the device. Two types of CuSCN-assisted devices were studied in this work. One was based on deposition of an ultrathin CuSCN layer between the perovskite absorber layer and the carbon cathode (PSK/CuSCN/C), and the other was by infiltrating CuSCN solution into the carbon film (PSK/C-CuSCN) by taking advantage of the macroporous structure of the carbon. We have found that the CuSCN incorporation by both methods can effectively address the hysteretic feature in planar C-PSCs. The origin for the hysteresis evolution was unravelled by investigation of the energy alignment, kinetics of interfacial charge transfer and hole trap-state density. The results have shown that both types of CuSCN-contained devices showed improved interfacial charge carrier extraction, suppressed carrier recombination, reduced density of trap state and enhanced charge transport, leading to negligible hysteresis. Furthermore, the CuSCN-incorporated C-PSCs demonstrated enhanced device stability. The PCE remained 98% and 91% of the initial performance (13.6% and 13.4%) for PSK/CuSCN/C and PSK/C-CuSCN, respectively, after being stored under high humidity (75-85%) environment for 10 days. The devices also demonstrated extraordinary long-term stability with negligible performance drop after being stored in air (relative humidity: 33-35%) for 90 days.

KEYWORDS: *CuSCN, perovskite solar cells, carbon-based, stability, hysteresis*

1. Introduction

Organic-inorganic hybrid lead trihalide perovskite solar cells (PSCs) have shown great potential as a promising photovoltaic technology that delivers cost-effective solar electricity. The power conversion efficiency (PCE) for PSCs even surpasses the performance of traditional thin film solar cells and multicrystalline silicon cells [1]. The unprecedented progress of PSCs is attributed to the advancement in material engineering of morphology and composition of perovskite light absorption layer, optimized interfacial properties of perovskite/electron transport layer (ETL) as well as perovskite/hole transport layer (HTL) [2-4]. However, the critical issue of instability of PSCs under operational condition restricts commercialization of this technology in practice. In a state-of-the-art PSC device, organic hole transport materials such as spiro-OMeTAD [5] and noble metal counter electrode (Au or Ag) [6-8] are needed to extract charge. These materials are not only expensive but also unstable in air giving rise to device degradation. Carbon material is considered as an ideal candidate for PSCs due to its merits of low material cost, excellent material stability, suitable work function, strong mechanical properties as well as its relatively strong water resistant surface property [9]. Carbon has been extensively studied to fabricate HTL-free PSCs owing to its dual functions of charge extractive layer and current collector, after the pioneer work by Mei et al. [10] The current highest efficiency of 15.60% for HTL-free C-PSCs was reported [11]. In the meantime, to improve hole extractive ability of carbon materials, NiO was introduced into C-PSCs, which has led to a record performance of 17.02% for the organic HTL-free based C-PSCs [12].

However, although rarely being discussed, most carbon based PSCs suffer from severe hysteresis phenomenon with obvious “bump” in the current density-voltage (*J-V*) plot of the device. The hysteresis behaviour can be caused by both external testing condition and intrinsic properties of the device. For example, the degree of hysteresis relies on the scan rate, scan direction (reverse scan vs forward scan) and preconditioning treatment (in the dark or under illumination) used in the photovoltaic performance measurement of the PSCs [13]. This raises the issue of reliability of device performance in practice. Fundamentally, hysteresis is caused by the imbalanced charge extraction at the two interfaces of perovskite/HTL and perovskite/ETL due to the different charge extraction ability. Therefore the interfacial contact quality between the perovskite layer and the charge extract layer is highly important to reduce or even eliminate the hysteresis behaviour of PSCs [14-16]. Attempts have been made to improve interfacial contacts in C-PSCs. Rong et al. [17] have reported that the hysteresis of mesoporous carbon based C-PSCs could be tuned by changing the thickness of TiO_2 based ETL compact layer used in the device.

A hysteresis-free feature was achieved with two layers of TiO_2 film. Zimmerman et al. [18] showed that adding CuSCN into perovskite precursor solution could form a bulk heterojunction of perovskite and CuSCN mixed layer. The modified perovskite absorber layer showed improved efficiency and reduced hysteresis in printable mesoporous carbon based PSCs due to the shorter hole extraction distance within the relative thick devices. Nevertheless, engineering the interface between perovskite layer and carbon film, which may also has significant effect on hysteresis behaviour of C-PSCs, has largely been unexplored.

It is well-known that there is a large energy offset between the valence band of perovskite absorber layer (normally ranging from -5.9 eV to -5.4 eV [19]) and carbon electrode (the Fermi level is around -5.0 eV [10]), which could impact interfacial hole transfer efficiency, resulting in imbalanced charge extraction and thus anomalous hysteretic behaviour. The abundant study on PSCs with conventional architecture of ETL/perovskite/Spiro-OMeTAD/Au has shown the device hysteresis behaviour can be controlled by optimizing the interface of perovskite/HTL to acquire better energy level alignment and charge extraction[20-22]. Theoretically speaking, inserting a hole transport material with suitable energy level to match both the valence band of perovskite and the work function of carbon could reduce the hysteresis of C-PSCs. Copper thiocyanate (CuSCN) as an inorganic p-type semiconductor possesses properties of large band gap, high mobility, most importantly, valence band of -5.2 eV that can better match the energy level alignment of perovskite and carbon [23-24]. In addition, compared to other inorganic hole transport materials, an uniform thin CuSCN layer can be achieved by solution process at low temperature. Therefore, it is a suitable materials for C-PSCs. Moreover, there is huge potential for carbon based planar PSCs in practice because it can be fabricated at low temperature using cost-effective procedure such as roll-to-roll. Thus it is of great significance to understand the interfacial properties of carbon/perovskite and their correlation with device hysteresis.

In this work, we investigated the effect of CuSCN on efficiency, hysteresis and stability of carbon-based planar perovskite solar cells made by doctor blading at low temperature by either inserting the CuSCN layer between the layer of perovskite and carbon film (denoted as PSK/CuSCN/C) or by filling the mesoporous carbon film with CuSCN solutions (named as PSK/C-CuSCN). We have found that, compared to the C-PSCs without CuSCN, the CuSCN containing devices by both methods showed reduced or eliminated *J-V* hysteresis of the devices. Further characterisation have shown the presence of CuSCN material led to improved energy alignment between perovskite and carbon, reduced density of trap state, enhanced carrier extraction and inhibited carrier recombination as well as decreased hole trap-state density. In

addition, the CuSCN was also found to enhance the hydrophobicity of the PSCs. These beneficial features contributed to the eliminated hysteresis and improved device stability against moisture. Our work also suggests that compared to PSK/C-CuSCN, PSK/CuSCN/C is more efficient to address the hysteresis and stability of C-PSCs owing to the enhanced interfacial charge transport.

2. Experiment section

2.1 Materials preparation

All materials were purchased from Sigma-Aldrich and used as received without further purification unless otherwise stated. Materials for the preparation of triple cation perovskite film, such as ammonium bromide (MABr) and formamidinium iodide (FAI) were provided by Dyesol, ltd. Lead iodide (PbI_2, 99.99%) was purchased from Alfa Aesar and the carbon paste was provided from Guangzhou Saidi Technology co. ltd, China.

2.2 Device assembly

Fluorine-doped tin oxide (FTO) glass substrates (Nippon Electric Glass, 15 Ω square^{-1}) were partially etched by using 35.5 wt% hydrochloric acid (HCl) and zinc powder. Then the patterned substrates were cleaned in 5% Decon-90 detergent water under ultrasonic bath for 20 min and rinsed with deionized water, followed by sonication of a mixture of ethanol, isopropanol and acetone with volume ratio of 1:1:1 for 20 min. After this, the FTO substrate was dried by blow-nitrogen gas and treated with ultraviolet-ozone (UV-ozone) for 30 min to completely remove the residual organic solvent. A dense electron transport layer of tin dioxide (SnO_2) was deposited on the top of FTO-coated glass through spin-coating 0.1 M tin (II) chloride ($SnCl_2$) solution in ethanol at 3000 rpm for 30 s. The film was dried at 100 °C for 5 min and annealed at 185 °C for 1 h in a muffle furnace. The SnO_2 based substrates were further treated under UV-ozone for 30 min, before being transferred into an N_2-filled glove box.

The triple cation perovskite ($Cs_{0.05}FA_{0.83}MA_{0.17}PbI_{2.53}Br_{0.47}$) precursor was prepared by a mixed solution containing MABr (0.2 M), FAI (1.0 M), $PbBr_2$ (0.2 M) and PbI_2 (1.1 M) in anhydrous dimethylformamide (DMF) and dimethylsulphoxide (DMSO) (v/v = 4:1), and CsI solution (5% volume, 1.5 M DMSO). The perovskite films were deposited onto the SnO_2-coated substrates by a spin-coating method in a two-step procedure including deposition at 1000 rpm for 10 s and then at 6000 rpm for 30 s. During the second programme, the perovskite layer was quenched by dropping 150 μl of chlorobenzene on the spinning substrate at 17 s

before the end of this step. Thereafter, the perovskite films were heated on a hot plate at 100 °C for 45 min. After cooling down to room temperature, the carbon paste was coated onto the perovskite film by doctor blading method. Eventually, the devices were transferred to a vacuum oven and dried for 30 min at 100 °C.

To make perovskite/CuSCN/C based cell, a copper thiocyanate (CuSCN) film was deposited by dynamic dripping method reported previously [25]. Specifically, 35 µl CuSCN precursor solution prepared by adding 35 mg CuSCN in diethyl sulfide (DES) was drop casted onto the spinning perovskite layer at 5000 rpm within 2 s to yield a flat and thin film. After this, the carbon film was deposited by doctor-blading carbon paste. For the perovskite/C-CuSCN based device, the CuSCN solution was loaded on the top of carbon layer for 1 min to allow it to infiltrate into pores of the carbon film, before it was spin coated at 4000 rpm. Subsequently, the film was blow-dried by N_2 gas and washed by fast drop casting DES to remove excess CuSCN.

2.3 Characterization

The top-view and cross-sectional scanning electron microscopy (SEM) images of the samples were captured by using a field emission scanning electron microscope (FSEM JOEL 7001 F) at an acceleration voltage of 5 kV and 10 kV. The cross-sectional elemental line scan spectrum of the samples were characterized at an acceleration voltage of 20 kV by FSEM JOEL 7001 F combined with an energy-dispersive X-ray spectroscopy (EDS). X-ray diffraction pattern (XRD. Rigaku Smartlab) of the film coated on FTO-glass substrates or solid powder samples were obtained using a monochromatic CuKα ($\lambda = 0.154$ nm) as a radiation source. The scan rate and step size used in the XRD measurement were 1.5 °/min and 0.02 °, respectively. X-ray photoelectron spectroscopy (XPS) and ultraviolet photoelectron spectrum (UPS, HeI as resonance line, photo energy is 21.22 eV) were obtained via Kratos AXIS Supra photoelectron spectrometer. UV-visible absorbance spectrum of the samples was measured by a UV-visible spectrometer (Carry 60). Photoluminescence spectrum was recorded with a spectrofluorometer. The samples were excited with 450 W Xenon lamp at a fixed wavelength of 487 nm and the photo emission was recorded in the range of 500 to 900 nm.

The performance of perovskite solar cells was measured under irradiation of 100 mW/cm^2 (AM1.5, 1 sun) provided by a solar simulator (Oriel Sol3A, Newport) equipped with 450 W Xenon lamp. The active area of the devices was 0.115 cm^2 with a black mask to block light scattering. External quantum efficiency (EQE) spectrum was tested with a quantum efficiency

measurement system (IQE 200B, Newport) under AC mode. Transient V_{oc} and J_{sc} measurement under light/dark cycling was achieved by switching on and off light illumination simulator (1 sun intensity) every 100 seconds. Electrochemical impedance spectroscopy (EIS) of the devices was performed in a frequency range from 1 MHz to 100 mHz via an electrical workstation (VSP BioLogic Science Instruments) under open-circuit condition with different illumination intensities. The light intensity dependence of open-circuit voltage (Voc) test was recorded through testing *J-V* curves of perovskite cells under different light illumination intensities by using neutral density optical filters. Impedance spectroscopy (IS) measurement was performed in the dark for a cell area of 1.4 cm^2. Hole trap-state density of film was achieved by dark *J-V* technique for hole only device. *J-V* scans for the devices were measured under 1 sun illumination with different scan rates of 50 mV/s, 140 mV/s, 200 mV/s and 300 mV/s, respectively.

The long-term stability of PSCs was measured by monitoring the device performance without encapsulation stored in a desiccator (humidity: around 30-35%) under dark condition. Photovoltaic performance of the cells in ambient environment were also tested with humidity of 50-70%. The stability of device in high humidity environment was performed in a moisture chamber with humidity around 75-85% and the *J-V* performance was periodically recorded. Four samples for each type of devices were tested in terms of the device stability under both low (30-35%) and high (75-85%) humidity level. The hydrophobicity of the samples was measured by measuring the contact angle using First Ten Angstroms dynamic contact angle analyser (FTA 200) at ambience condition. The dosing volume of water droplet was 13 µl.

3. Results and discussion

Figure 1(a)-(d) illustrates the top-view scanning electron microscopy (SEM) images of $CsFA_{0.83}MA_{0.17}PbI_{2.53}Br_{0.47}$ perovskite, CuSCN coated perovskite, carbon layer and CuSCN coated carbon film, respectively. The perovskite film (Figure 1a) consists of crystal grains with size of 100-400 nm which are connected closely with each other thereby fully covering the underlying electron transport layer. This highly dense and flat surface of perovskite layer is critical to device performance. After deposition of the CuSCN layer, the SEM image of the film becomes blurred (Figure 1b), due to the ultrathin thickness and inferior conductivity of CuSCN layer. The crystal structure of the perovskite layer and CuSCN was characterized by X-ray diffraction (XRD). As shown in Figure S1, the main peaks of the film at 14.1°, 28.4° and 31.9° are assigned to (101), (202) and (211) lattice planes of perovskite, respectively [26-27]. As for the CuSCN pattern, normally, CuSCN has two different polymorphs known as α-CuSCN

and β-CuSCN. The CuSCN used in this work is mainly composed of β-CuSCN, which has hexagonal crystal structure [25, 28].

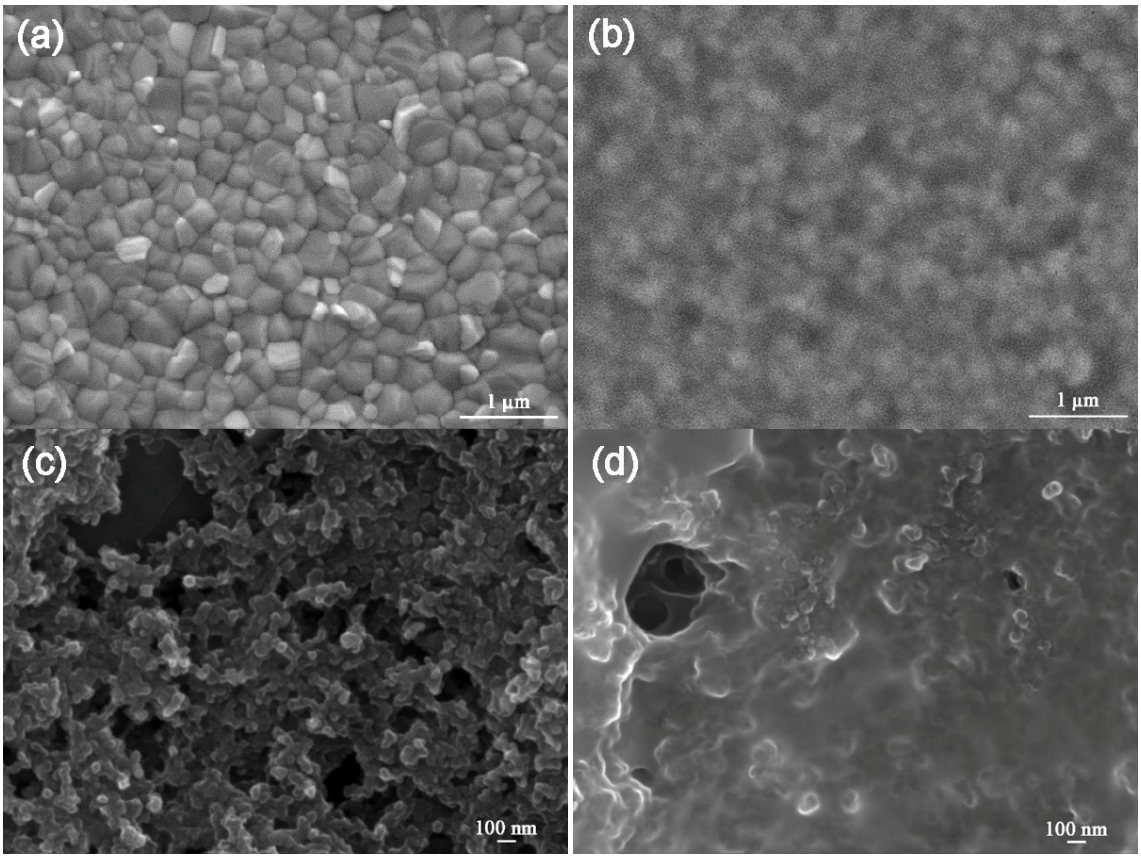

Figure 1. Top-view SEM images of (a) $Cs_{0.05}FA_{0.83}MA_{0.17}PbI_{2.53}Br_{0.47}$ film, (b) CuSCN film on the top of perovskite layer, (c) carbon layer and (d) CuSCN film on top of carbon layer.

Figure 1c shows the surface of carbon layer fabricated by doctor blading. It is obvious that the film consists of carbon nanoparticles and has mesoporous structure. Meanwhile, the presence of cracks is evident in the film as shown at low magnification (Figure S2). These holes and cracks provide the tunnels for permeation of moisture and oxygen, causing perovskite decomposition. However, after deposition of a CuSCN thin layer onto the carbon film (Figure 1d), the majority of holes of the carbon film were filled, forming a super thin passivation layer to block transport of moisture to perovskite. To estimate the thickness of each layer, cross-sectional SEM images of the PSC devices (Figure 2) were acquired. It indicates approximately 500 nm for the perovskite layer, 50 nm for CuSCN layer and 15 μm for carbon layer, respectively. Compared with pure carbon layer (Figure 2a and 2b), the CuSCN-carbon mixed composite layer presents a dense feature as shown in Figure 2c where CuSCN permeated into the carbon and fiercely glued the porous carbon particles and graphite together.

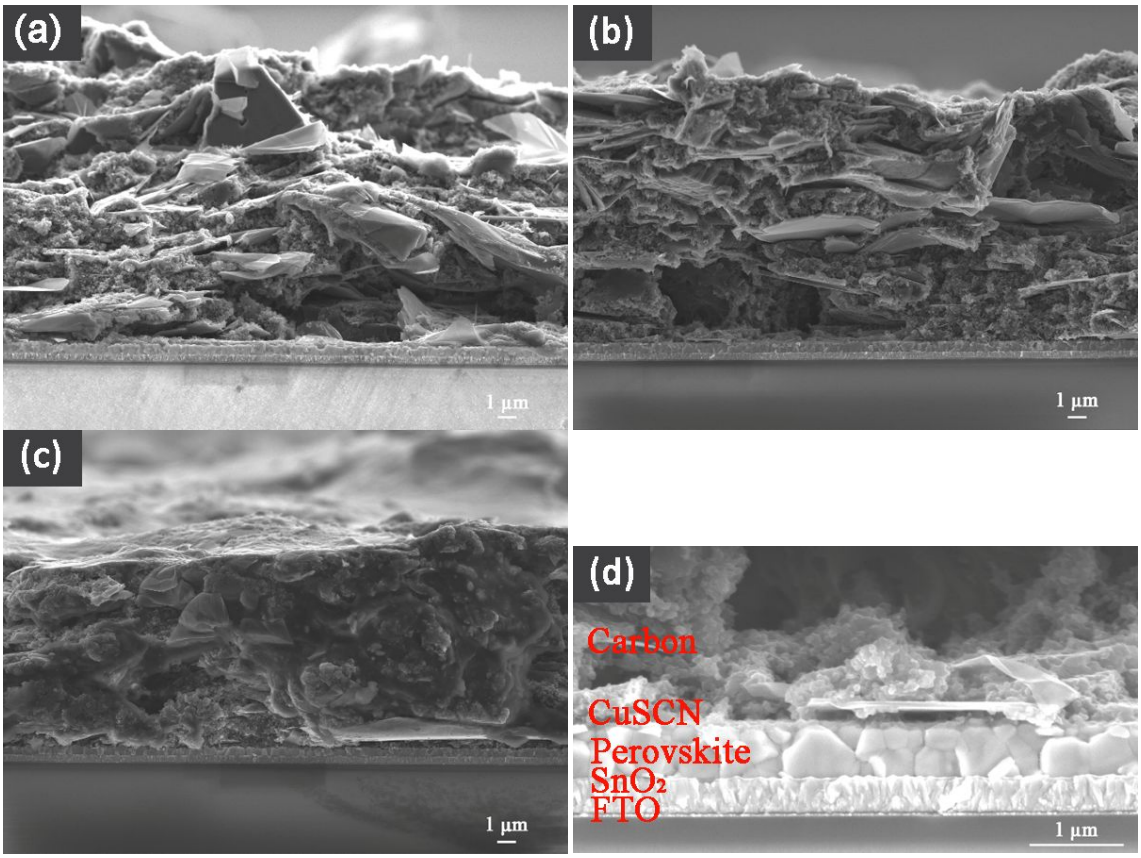

Figure 2. Cross-sectional SEM images of (a) PSK/C, (b) PSK/CuSCN/C, (c) PSK/C-CuSCN and (d) PSK/CuSCN/C at high magnification.

In order to determine the existence and distribution of CuSCN, X-ray photoelectron spectroscopy (XPS) and energy-dispersive X-ray spectroscopy (EDS) of the films were obtained. XPS pattern (Figure S3) demonstrates that there is only C in the carbon layer. In addition, some weak peaks of Cu and S can be found in the carbon-CuSCN based film, revealing small amount of CuSCN located on the surface of carbon. EDS line scan spectra (Figure S4) of the PSK/C-CuSCN cell confirms that CuSCN is rich on top of carbon layer which reduces gradually into the carbon. By contrast, the CuSCN layer sandwiched between the perovskite layer and the carbon electrode does not show observable inter-diffusion to other layers (Figure S5).

Ultraviolet photoelectron spectrum (UPS) was employed to assess the energy band alignment between perovskite/CuSCN/C and perovskite/C-CuSCN in the devices. As depicted in Figure 3a, the cut-off binding energy for the CuSCN layer is 16.63 eV, whereas the cutting off energy is around 16.92 eV for perovskite. As for carbon based films, there is a small

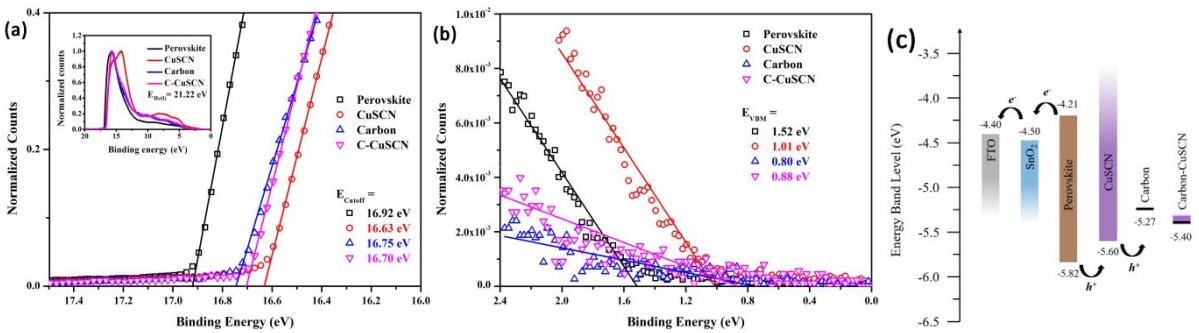

Figure 3. (a) Ultraviolet photoelectron spectra positioning cutoff edge of perovskite, CuSCN, carbon and carbon-CuSCN films. Insert: UPS spectrum of different layers. (b) Valence band maximum (VBM) of various films obtained from UPS. (c) Calculated energy band level in accordance with the UPS and UV-vis spectrum results.

difference between pure carbon layer with the value of 16.75 eV and CuSCN coated carbon which has a lower value, about 16.70 eV. The valence band maximum (VBM) of the films can be determined by fitting the linear part of the high kinetic energy curve close to the Fermi edge (Figure 3b). It is found that CuSCN has a small E_{VBM} value of 1.01 eV, which is approximately 0.5 eV lower than perovskite. Besides, after depositing CuSCN on carbon, its E_{VBM} increases mildly from 0.80 eV for pristine carbon to 0.88 eV. The energy position of valence band (E_{VB}) for these films was calculated, according to the equation below.

$$-E_{valence\ band} = E_{He(I)} - E_{cutoff} + E_{VBM} \quad (1)$$

Combined with the band gap value obtained from UV-visible absorption spectrum (Figure S6) of perovskite layer, the energy band level of materials utilized in the devices are estimated in Figure 3c. It is found that the E_{VB} of CuSCN is higher than that of perovskite but lower than carbon. This creates a cascade for efficient hole separation and extraction from perovskite to CuSCN before being collected by carbon electrode. With the deposition of CuSCN on top of carbon layer, the E_{VB} for the carbon-CuSCN composited film is downward shifted to -5.40 eV, which is more close to that of perovskite. The modification of E_{VB} enables more efficient hole transport and reduce carrier recombination at the interface between the perovskite and the carbon. In comparison to the PSK/C-CuSCN based cell, the produced hole consumes more energy to jump directly from the perovskite to the pure carbon for PSK/C based device. The electron and hole transport mechanism can be depicted as that the hole transport can only be achieved from layer to layer in PSK/CuSCN/C, which means the tunnelling effect of hole transport given the thickness of CuSCN is very thin. However, when it comes to PSK/C-

CuSCN structure, the naturally formed tunnels filled with CuSCN supply the second way for transport and collection of hole carriers.

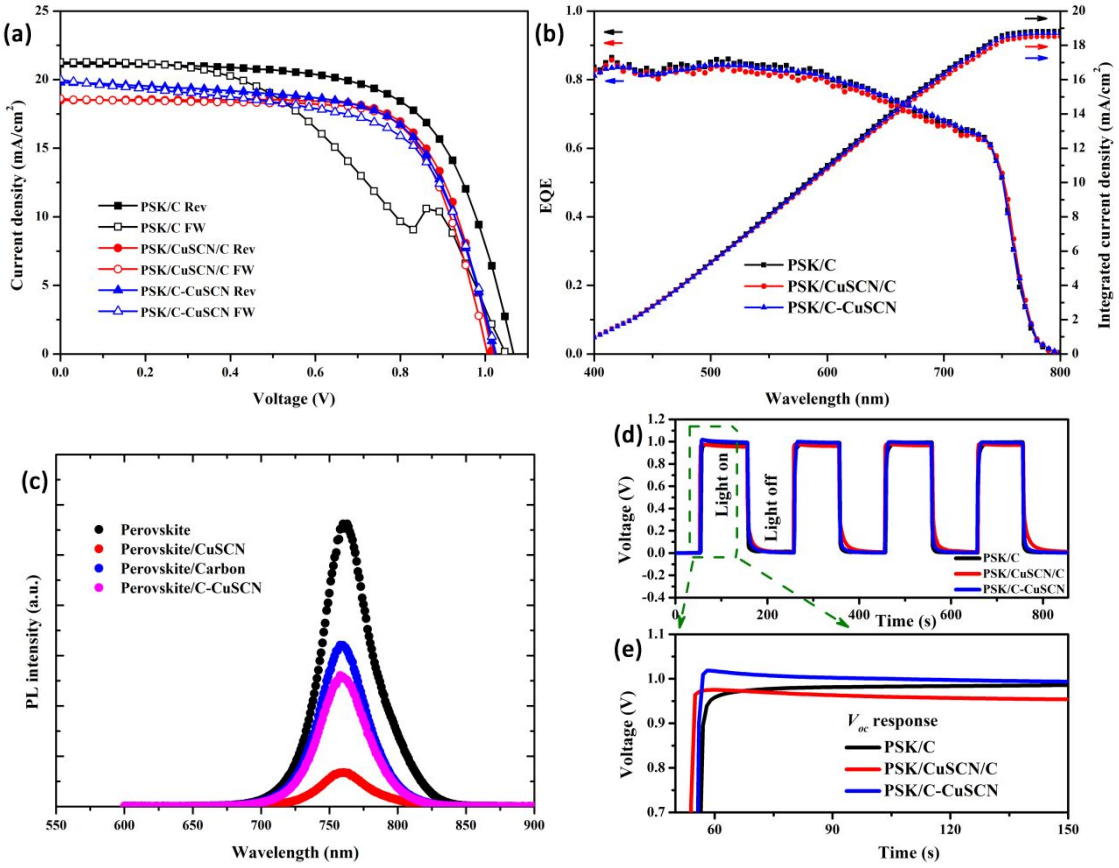

Figure 4. (a) *J-V* curves of different perovskite solar cells measured under reverse and forward scans. (b) EQE spectrum of various types of cells. (c) Steady-state PL spectrum of different films. Excitation wavelength is 487 nm. (d) Transient voltage measurements for different devices under cyclic illumination. (e) The enlarged views of (d).

The *J-V* curves of the three types of devices, PSK/C, PSK/CuSCN/C and PSK/C-CuSCN, were recorded under irradiation of 100 mW/cm^2 (AM1.5, 1 sun) by a solar simulator (Figure 4a). The corresponding characteristics performance parameters are summarised in Table 1, including open-circuit voltage (*Voc*), short-current density (*Jsc*), fill factor (*FF*), power conversion efficiency (PCE) and hysteresis index (HI). In particular, the PSK/C based device displays an outstanding PCE of 14.8% in the reverse scan for the champion cell with a high *Voc* of 1.07 V and an impressive *Jsc* of 21.17 mA/cm^2, respectively. Nevertheless, due to the poor fill factor, the hysteresis behaviour is significant with the device and there is a small "bump" in the *J-V* curve at around 0.9 V in the forward scan. The main reason for this behaviour is caused by inferior hole extraction and poor interfacial contact at the interface of

perovskite/carbon, which affect charge carrier transport. In addition, owing to the large energy offset between perovskite and carbon, when a high external voltage bias is applied to PSK/C, the Fermi level of electrons raises toward the conduction band thereby causing the carrier and ion accumulation at the interface. This charged accumulation space deters hole injection and forms a capacitance across the interface leading to the "rough" *J-V* curve [29]. In contrast, the CuSCN contained device shows negligible hysteresis but with slightly lower efficiency with 13.6% for PSK/CuSCN/C and 13.4% for PSK/C-CuSCN. Figure S7 summarizes the statistical photovoltaic parameters of 20 cells for each type of PSCs which shows similar trend with the best device. We can conclude that the introduction of CuSCN to the device reduces both *Voc* and *Jsc* of the cells slightly, but increases FF in both forward and reverse scan, leading to suppressed hysteresis. The decrease of *Voc* and *Jsc* is induced by the marginally higher monomolecular recombination happening inside of the CuSCN based cells [25]. Based on *J-V* measurement results, it is assumed that indeed carbon materials possess charge extractive ability from the organo-metal perovskite although its hole extraction ability is not sufficiently high due to less ideal energy alignment and lower electrical conductivity, which in turn can affect hysteresis of the device. After incorporating with CuSCN to help enhance the hole transport, the hysteretic feature is reduced or even eliminated. The external quantum efficiency (EQE) spectrum of the PSCs was obtained to check the integrated photo-current density (Figure 4b). All the curves exhibit high EQE, around 80%, across a wide range of wavelength from 400 to 650 nm. The onset wavelength at approximately 780 nm is in agreement with the bandgap of perovskite layer. The integrated *Jsc* of CuSCN-assisted devices calculated from

Table 1. Characteristic photovoltaic parameters of different types of devices under reverse and forward scans.

sample	scan direction	V_{oc} (V)	J_{sc} (mA/cm^2)	FF (%)	PCE (%)	R_s (Ω cm^2)	R_{sh} (kΩ cm^2)	HI[a]
PSK/C	Rev	1.07	21.17	65.4	14.8	64.5	5.6	0.331
	FW	1.04	21.34	44.6	9.9	107.0	2.6	
PSK/CuSCN/C	Rev	1.02	18.49	72.1	13.6	55.6	63.3	0.015
	FW	1.00	18.58	71.6	13.4	63.3	13.4	
PSK/C-CuSCN	Rev	1.02	19.83	66.0	13.4	69.1	6.0	0.052
	FW	1.03	19.93	62.3	12.7	69.2	2.8	

[a]Hysteresis index = $(PCE_{Rev} - PCE_{FW})/PCE_{Rev}$

EQE are 18.46 mA/cm^2 for PSK/CuSCN/C and 18.64 mA/cm^2 for PSK/C-CuSCN, respectively, which are very close to the *Jsc* measured from the *J-V* curve. However, the calculated *Jsc* of pure carbon based cell is 18.78 mA/cm^2, which is much lower than the *Jsc* value in *J-V* plot. This difference is attributed to the presence of abundant shallow trap states at the interface between the perovskite and the carbon layer [30], which could be filled up under high illumination used in the *J-V* measurement but not in the quantum efficiency spectrum. The steady-state photoluminescence (PL) spectrum (Figure 4c) illustrates the strong PL emission of perovskite film at about 763 nm. When the perovskite is in contact with CuSCN, its PL is significantly quenched. Based on this, we can infer a rapid hole extraction occurring at the perovskite/CuSCN interface [31]. Similarly, the PL intensity of carbon-CuSCN composite film/perovskite is apparently lower compared to perovskite/carbon sample, indicating a more efficient carrier extraction.

Figure 4d exhibits V_{oc} response of the PSCs under light/dark cycle. It is clearly shown that the devices with CuSCN present much faster response than the HTM-free cell. The zoomed-in plot of the first transient V_{oc} cycle (Figure 4e) implies that the V_{oc} of CuSCN assisted cells reaches to the maximum value within less than 5 s. In contrast, the PSK/C based device needs around 20 s to achieve a stable V_{oc}. In the meantime, there is a visible distinction in response time between various cells under dark condition. The V_{oc} of PSK/C based device falls rapidly back to static state whereas for CuSCN based cells, they show obvious voltage decay. The longer V_{oc} decay under light-off condition indicates longer lifetime for the charge carriers and lower interface recombination rate [32]. The persistent voltage at low potential is caused by the slow back carrier transfer from ETL or HTL to perovskite layer that deters photovoltage back to dark equilibrium [33]. Clearly, the interfacial modification by CuSCN contributes to the elongation of carrier lifetime and the reduction of interfacial recombination. Normally, PSC devices with low hysteresis possess rapid response times to V_{oc}, which can be explained by slow release of the trapped charge carries and ions [34]. Therefore, the CuSCN layer plays the role to passivate the defects and reduce charge carries trapping at the interface of perovskite/carbon. Because fewer carriers and ions are captured and then released, a faster response to V_{oc} is accomplished, which directly contributes to the negligible hysteresis.

Furthermore, the series resistance (R_s) (Table 1) of the devices are found to decrease from 64.5/107.0 Ω cm^2 (reverse scan/forward scan) for PSK/C to 55.6/63.3 Ω cm^2 for PSK/CuSCN/C when inserting a CuSCN layer between perovskite and carbon film. For PSK/C-CuSCN based cell, the R_s also decreases to 69.1/69.2 Ω cm^2. The declined R_s implies

lower contact resistance and better conductivity of the interface between perovskite and carbon ascribed to the utilization of CuSCN. Meanwhile, the shunt resistance (R_{sh}) shows opposite trend. R_{sh} increases from 5.6/2.6 kΩ cm^2 for PSK/C to 66.3/13.4 kΩ cm^2 for PSK/CuSCN/C. In comparison, R_{sh} of PSK/C-CuSCN based cell just increase mildly to 6.0/2.8 kΩ cm^2, which denotes the similar charge recombination to pristine carbon cell. This results suggest CuSCN in direct contact with the perovskite indeed helps to reduce recombination in the traps and resistance of charge transport.

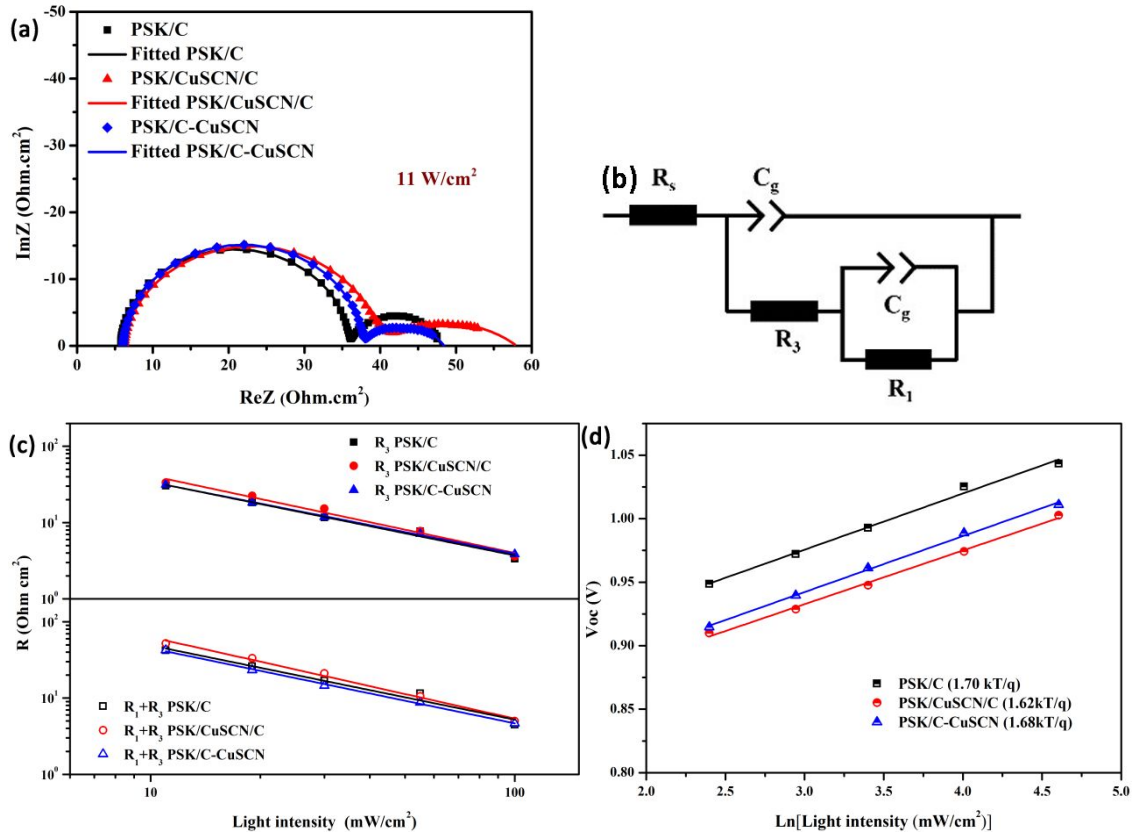

Figure 5. (a) Nyquist plots of perovskite/carbon cell, perovskite/CuSCN/carbon cell and perovskite/carbon-CuSCN cell under 11% AM 1.5G 1 sun light illumination and (b) the equivalent circuit. (c) Extracted resistance as a function of illumination intensity. (d) Open-circuit voltage (V_{oc}) as a function of light illumination intensity.

On account of the variation of series resistance and shunt resistance for PSCs, we further measured electrochemical impedance spectroscopy (EIS) of the PSCs at open-circuit condition (*Voc* bias) with different light illumination intensities (Figure S8) to understand the dynamic process of charge transfer and recombination of the devices. As exhibited in Figure 5a, there are two semi-circles in the Nyquist plot, which can be fitted with the equivalent circuit (Figure

5b). The first semi-circle at high frequency is associated with the capacitance, C_g, revealing the dielectric property of perovskite absorption layer and the resistance, R_3, which is mainly related to the transporting resistance of charge carrier at the interface of perovskite film and contacting layer. The second semi-circle at low frequency zone reflects the information of capacitive element C_s and resistive element R_1. In particularly, the sum of R_1 and R_3 is regarded as recombination resistance at interfaces [35-37]. It is found that there is no significant change of R_3 for all of these PSCs under the same light illumination (Figure 5c). Nonetheless, when we compare R_3 at the same *Voc*, the values for CuSCN assisted devices (Figure S9) are significantly lower than that for pure perovskite/carbon based cell, indicating higher efficiency of carrier transport due to better energy levels matching between perovskite layer and HTM layer. Figure 5c (bottom) illustrates that the recombination resistance (R_1+R_3) of PSK/CuSCN/C based cell is slightly higher than that for the other two types of devices at the same illumination intensity, which signifies ultrathin CuSCN can passivate carrier recombination at the interface between perovskite and carbon layer. This result is in agreement with the highest R_{sh} for PSK/CuSCN/C obtained from *J-V* measurement.

Moreover, the ideality factor for all of these PSCs are calculated by analysing the plot of open-circuit voltage versus light illumination intensity (Figure 5d) according to the following equation [38].

$$V_{oc} = \frac{m_\Phi k_B T}{\mathrm{q}} \ln (\Phi_{ph}) \quad (2)$$

Where q, k_BT and Φ_{ph} are elementary charge, thermal energy and absorbed light flux, respectively. The fitted m_Φ for PSK/C based cell is 1.70, which exceeds the value of 1.62 for PSK/CuSCN/C but similar to that for PSK/C-CuSCN based device (m_Φ = 1.68). Generally, the higher m_Φ suggest a more severe recombination at the interfaces. This indicates that the carrier recombination at the interface of perovskite absorbing layer and carbon electrode is reduced as a result of the incorporation of CuSCN. The results obtained from the ideality factor is consistent with the results of R_{sh} and R_1+R_3 of the CuSCN assisted devices showed above.

To further investigate the hysteresis behaviour, we measured *J-V* for the devices under light condition at various scan rates ranging from 50 to 300 mV/s. Normally, hysteresis can be aggravated with the increment of sweep rate, since it is really tough for mobile ions to move fast enough to follow the built-in electrical field of the device [39-40]. As shown in Figure S10, the PSC without CuSCN always shows apparent hysteresis behaviour regardless of the scan rates, and possesses the most serious hysteretic phenomena among the cells. This prevents the

device from producing a sustainable and steady output power at the given voltage point during *J-V* measurement. In contrast, there is almost no strong hysteresis for the PSK/CuSCN/C based device at different scan rates (Figure S10b). The hysteretic feature for PSK/C-CuSCN gradually fades with the increase of scan rates (Figure S10c). In particular, at the low sweep rate of 50 mV/s, eliminated hysteresis was detected. Interestingly, when using a small scan rate, 50 mV/s, CuSCN assisted cells present an inverted hysteretic patterns (HI < 0), mainly owing to the reduced FF at reverse scan (Figure S11). Similar to pervious reports [41-42], we assume this anomalous *J-V* hysteresis behaviour of PSCs is related to ion motion and the build-up of a space charge region at the interface between perovskite and CuSCN. If the slow sweep is applied, ions can be driven away from the space charge layer by the forward bias and diffuse

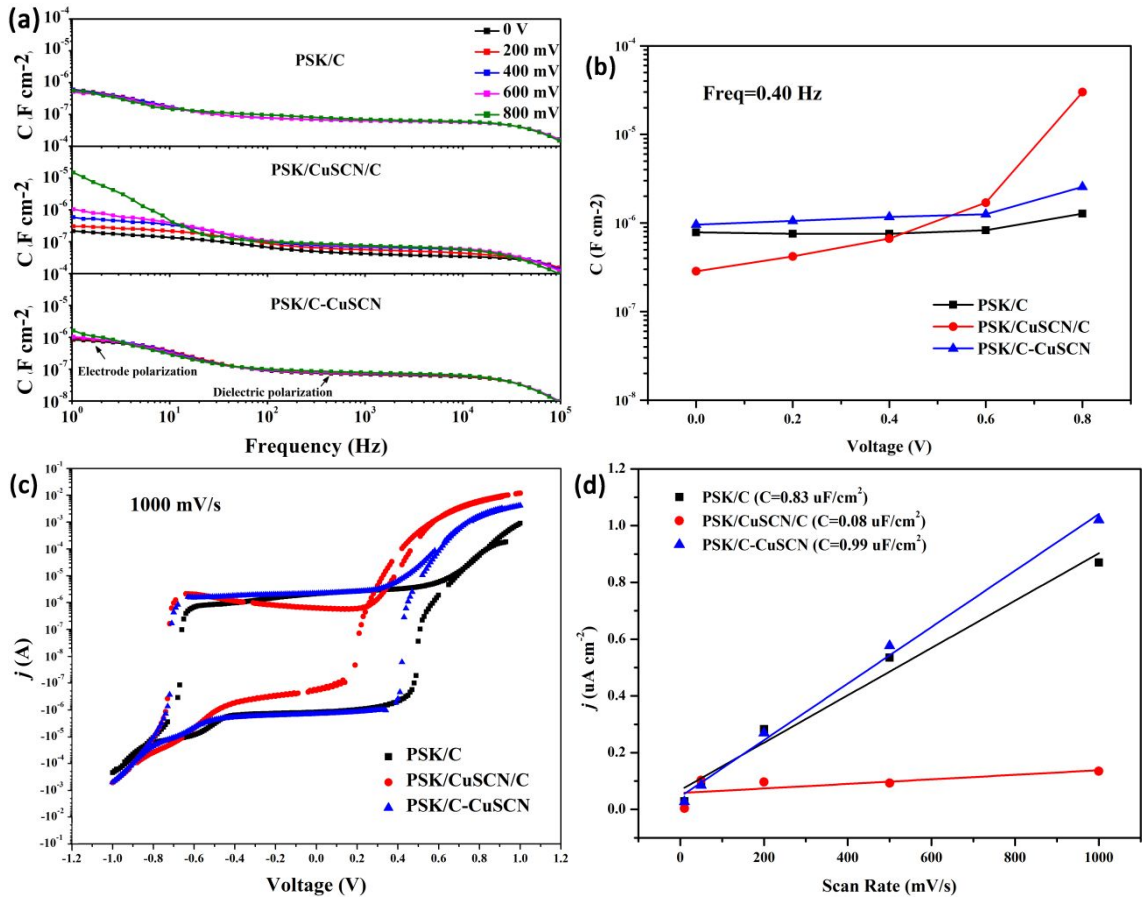

Figure 6. (a) Capacitance versus frequency plot of three different PSCs attained from electrochemical impedance spectra in the dark measured at various voltage bias. (b) Extracted *C-V* plot in the low frequency of 0.40 Hz. (c) Current vs voltage curves measured in the dark at the scan rate of 1000 V/s. (d) Calculated capacitance obtained from the linear fit of current vs scan rate plot tested in the dark without voltage bias.

into light absorption layer which will increase the charge recombination rate, thereby leading to low fill factor.

We further conducted IS measurements for these PSCs in the dark to understand charge accumulation at interfaces. The capacitance spectrum of the devices is illustrated as Figure 6a. Apparently, two main plateaus which are associated with an electrode polarization domain and a dielectric polarization domain, respectively, can be recognised in the capacitance-frequency plot. Particularly, the dielectric polarization domain at high frequency corresponds to the capacitance of C_g, which implies the bulk property of the perovskite layer and the electrode polarization domain at low frequency is associated to the capacitance of C_s indicating ion accumulation at the interfaces [42-43]. All of the devices present a relatively stable plateau at high frequency, but behave distinctively at the low frequency region. The low-frequency capacitance is just 0.21 μF/cm^{-2} at 1 Hz without bias and increases nearly two orders of magnitude to a relatively large capacitance of 14.80 μF/cm^{-2} at 800 mV for PSK/CuSCN/C based cell. In contrast, the device without CuSCN presents a typical ionic capacitance of 0.61 μF/cm^{-2} at 1 Hz and this value keeps largely constant regardless of the voltage bias applied. Interestingly, as for PSK/C-CuSCN, the capacitance value slightly grows up at high voltage bias (800 mV), thanks to the small amount of CuSCN, which modifies contact property between perovskite and carbon. Likewise, the ionic accumulation is very small for PSK/CuSCN/C based PSC with value in the range of 0.29 ~ 0.67 μF/cm^{-2} in the frequency range from 0 V and 400 mV at 0.40 Hz (Figure 6b). On the other hand, the capacitance of PSK/C and PSK/C-CuSCN based devices are always relatively higher in the whole voltage range, which can be interpreted as the evident ionic accumulation at perovskite/carbon interface induced by electrode polarization.

The cyclic voltagram is to identify capacitive current derived from ion migration [39, 44]. Generally speaking, under dark condition, the capacitive current is linearly correlated to the scan rate [45]. Hence, the voltage-independent capacitance can be calculated by the following equation [42].

$$J_{cap} = \frac{\mathrm{dQ}}{\mathrm{dt}} = C\frac{\mathrm{dV}}{\mathrm{dt}} = Cs \qquad (3)$$

As shown in Figure 6c, for the PSK/CuSCN/C, at a very fast voltage scan cycling of 1000 mV/s, it displays a teeny-weeny capacitive current induced by migrating ions from electrode polarization. This value is remarkably lower than that of the PSK/C and PSK/C-CuSCN which present a quite similar J_{cap}, denoting more typical ionic capacitance. Additionally, a linear

dependence of capacitive current and sweep rate is observed in Figure 6d. After fitting the discrete points, the extracted capacitance values of 0.83 μF/cm^{-2} for PSK/C, 0.08 μF/cm^{-2} for PSK/CuSCN/C and 0.99 μF/cm^{-2} for PSK/C-CuSCN at 0 V, respectively, are confirmed. It is evident that the capacitive value of PSK/CuSCN/C based cell is almost two order of magnitude lower than others, which is in agreement with the extracted result from capacitance-frequency diagram (Figure 6b). Based on the results, we can confirm CuSCN layer can effectively hinder hysteresis and polarization by reducing interface recombination and faster charge extraction.

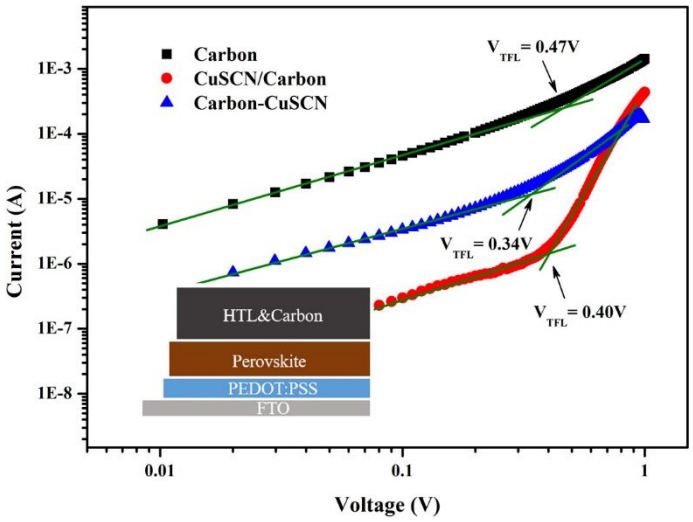

Figure 7. Logarithm of dark current-voltage curves for hole-only devices. Configuration of the device is shown in the insert.

Furthermore, we assembled hole-only devices to quantify the trap-state density for the CuSCN-assisted films. The logarithm of dark *J-V* curves for hole-only devices are demonstrated in Figure 7. The *J-V* curves in the dark normally can be divided into three parts. At the low-voltage region, the current presents a linearly climbing trend as a function of voltage, representing Ohmic conduction [46]. At the high-voltage region, beyond the turning point, the current increases nonlinearly, which is indicative to the fully filled trap state by the mean of carrier injection [47]. The trap-filling limited voltage (V_{TFL}) determined by the applied voltage at the turning point can be extracted from the curve and the trap-state density can be calculated using the equation as follow [48]:

$$V_{TFL} = \frac{eL^2 N_{trap}}{2\varepsilon\varepsilon_0} \quad (4)$$

Where L is the thickness of the film and e is the elementary charge. The relative dielectric constant of the film, ε, is around 35 [49] and the vacuum permittivity, ε_0, is 8.854 × 10^{-12} F/m.

The specific hole defect-state density are 7.28 × 10^{-15} cm^{-3} for PSK/C based device, 6.19 × 10^{-15} cm^{-3} for PSK/CuSCN/C based device and 5.27 × 10^{-15} cm^{-3} for PSK/C-CuSCN based device, respectively. It is clearly found that the trap density for CuSCN-assisted devices are lower in comparison to pristine perovskite/carbon based cell. That means the additive CuSCN

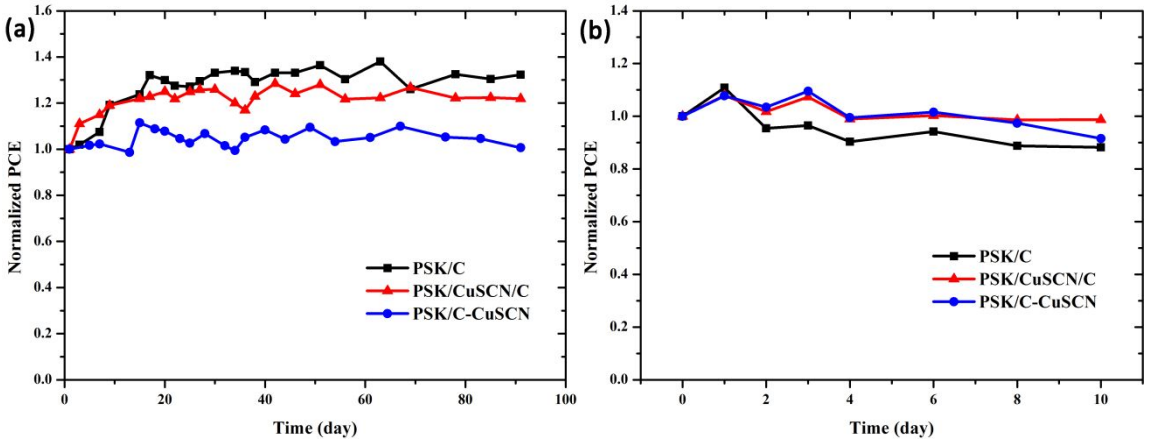

Figure 8. Normalised PCE obtained from reverse scan of various devices measured (a) over 90 days (storage condition, humidity: ~30-35%, temperature: ~23-27 C°), (b) around 10 days stored at high humidity (~75-85%).

is able to efficiently passivate carrier trap and compensate the defect-state density of the interface between perovskite and carbon.

The stability of these three types of PSCs were examined by monitoring the photovoltaic performance under various conditions. The long-term stability for all of the devices is impressive as shown in Figure 8a, where the performance increases gradually in the first several days to reach a relatively stable state. There are two main reasons to explain this trend. First of all, perovskite absorption layer is unique semiconductor material owning to ion migration that needs some time to reach the steady state [50]. In addition, oxygen is another external stimuli leading to the improvement of PSCs, since it has been proved that oxygen can interact with metal oxides and perovskite, but the process of oxygen permeation inside of the devices takes time [51-52]. After period, all the cells stay at the relatively high performance all along in spite of several trivial fluctuations over 90 days stored in dry air. Essentially, the hysteresis features for the CuSCN-assisted PSCs are still very small throughout the test, compared to the pure carbon based device whose hysteretic behaviour is always dramatic (Figure S12). Further test of the moisture stability for the devices (Figure 8b) illustrates that PSCs containing CuSCN enable to retard the degradation against high humidity. After aging for 240 hours at the high relative

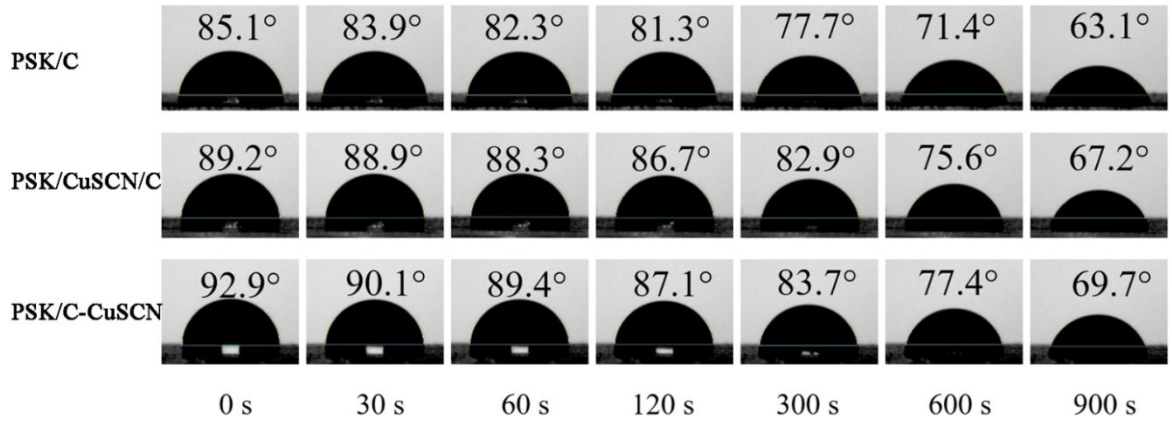

Figure 9. Profile of a water droplet on the surface of perovskite/carbon, perovskite/CuSCN/carbon and perovskite/carbon-CuSCN based cells over the period time of 15 min.

humidity of 75-85%, PSK/CuSCN/C based cells retained more than 98% of its initial efficiency but only 88% of original PCE was remaining for pure carbon device.

To further understand the improved stability, we monitored the contact angle (CA) of the films over the period time of 15 min to check the vulnerability of these devices to water (Figure 9). Generally, the CA variation of water droplet during the first 30 s is untrustworthy as it takes seconds for water droplet to spread out to fulfil an apparent static contact angle [16, 53]. After this stage, the further CA reduction is regarded as the penetration of water into perovskite layer [54]. The images of the water droplet deposited for 15 min suggest that the CuSCN-integrated carbon composite films are more hydrophobic than the pure carbon layer. Due to the mesoporous structure of carbon layer shown in SEM images, water droplet can easily infiltrate into the carbon film and reach to perovskite, causing degradation of the whole device. However, when we embedded a CuSCN layer in the middle of perovskite and carbon or fill CuSCN into the holes of carbon, it enables the repulsion of CuSCN-assisted carbon films against water from reaching to perovskite material, thereby enhancing the stability and robustness of PSCs. Actually, an ultrathin inorganic CuSCN layer does effectively protect perovskite layer from the moisture, as shown in Figure S13, where the CA of water drop dramatically increases from 49.4° to 80.2°.

3 Conclusions

We designed two different types of CuSCN-assisted carbon based PSCs by either inserting an ultrathin CuSCN layer between the interface of perovskite and carbon or filling CuSCN into the macroporous carbon film. The energy band alignment between perovskite and carbon was found to be improved due to the incorporation of CuSCN. Photovoltaic measurement results indicated the hysteresis and polarized behaviour of the CuSCN based devices can be effectively passivated as a result of the boosted charge carrier transport and hindered carrier recombination. Further investigation showed the PSCs containing CuSCN enable lower hole trap-state density of perovskite/carbon interface. Finally, a PCE of 13.6% (and 13.4%) with the negligible hysteresis was achieved in PSK/CuSCN/C (and PSK/C-CuSCN) based device. Moreover, owing to the nature of inorganic materials, the CuSCN-assisted devices exhibited robust resistance to moisture with the performance retention of 98% (PSK/CuSCN/C) and 91% (PSK/C-CuSCN) after storing 10 days at high humidity around 75-85% and superior long-term stability with the almost changeless PCE after 90 days. This work vigorously paves a new road to integrate inorganic hole transporting materials with carbon electrode to modify interfacial contact of perovskite/carbon and fabricate stable perovskite solar cells with eliminated hysteresis for commercial application in the future.

Acknowledgements

The authors thank the financial support to this work by Australian Research Council Discovery Project (DP190102252). Y.Y thanks Queensland University of Technology (QUT) postgraduate scholarship. L.J.F acknowledges the support by Chinese Scholarship Council (CSC). The data of XRD, SEM, EDX, XPS, UPS reported in this paper were obtained at the Central Analytical Research facility (CARF), QUT. Access to CARF was supported by the generous funding from Science and Engineering faculty, QUT.

Supporting Information

XRD data, SEM images, XPS spectrum, EDS line scan spectra, UV-vis absorption spectrum and water contact angle images of different films. Statistical photovoltaic parameters, EIS plots, *J-V* response at different scan rates and stability data for the devices.

Notes

The authors declare no competing financial interest.

References

(1) National Renewable Energy Laboratory USA. Best Research-Cell Efficiencies, **2019,** *https://www.nrel.gov/pv/assets/pdfs/best-research-cell-efficiencies-190416.pdf*.

(2) Zhou, H.; Chen, Q.; Li, G.; Luo, S.; Song, T.-B.; Duan, H.-S.; Hong, Z.; You, J.; Liu, Y.; Yang, Y. Interface Engineering of Highly Efficient Perovskite Solar Cells. *Science* **2014**, *345*, 542-546.

(3) Saliba, M.; Matsui, T.; Seo, J.-Y.; Domanski, K.; Correa-Baena, J.-P.; Nazeeruddin, M. K.; Zakeeruddin, S. M.; Tress, W.; Abate, A.; Hagfeldt, A. Cesium-containing Triple Cation Perovskite Solar Cells: Improved Stability, Reproducibility and High Efficiency. *Energy Environ. Sci.* **2016**, *9*, 1989-1997.

(4) Agresti, A.; Pescetelli, S.; Taheri, B.; Del Rio Castillo, A. E.; Cinà, L.; Bonaccorso, F.; Di Carlo, A. Graphene-Perovskite Solar Cells Exceed 18% Efficiency: A Stability Study. *ChemSusChem* **2016**, *9*, 2609-2619.

(5) Bi, D.; Tress, W.; Dar, M. I.; Gao, P.; Luo, J.; Renevier, C.; Schenk, K.; Abate, A.; Giordano, F.; Baena, J.-P. C. Efficient Luminescent Solar Cells Based on Tailored Mixed-Cation Perovskites. *Sci. Adv.* **2016**, *2*, No. e1501170.

(6) Bai, Y.; Meng, X.; Yang, S. Interface Engineering for Highly Efficient and Stable Planar p-i-n Perovskite Solar Cells. *Adv. Energy Mater.* **2018**, *8*, No. 1701883.

(7) Ali, F.; Pham, N. D.; Bradford, H. J.; Khoshsirat, N.; Ostrikov, K.; Bell, J. M.; Wang, H.; Tesfamichael, T. Tuning the Amount of Oxygen Vacancies in Sputter-Deposited SnOx Films for Enhancing the Performance of Perovskite Solar Cells. *ChemSusChem* **2018**, *11*, 3096-3103.

(8) Yang, Y.; Song, J.; Zhao, Y.; Zhu, L.; Gu, X.; Gu, Y.; Che, M.; Qiang, Y. Ammonium-Iodide-Salt Additives Induced Photovoltaic Performance Enhancement in One-Step Solution Process for Perovskite Solar Cells. *J. Alloys Compd.* **2016**, *684*, 84-90.

(9) Chen, H.; Yang, S. Carbon-Based Perovskite Solar Cells without Hole Transport Materials: The Front Runner to the Market? *Adv. Mater.* **2017**, *29*, No. 1603994.

(10) Mei, A.; Li, X.; Liu, L.; Ku, Z.; Liu, T.; Rong, Y.; Xu, M.; Hu, M.; Chen, J.; Yang, Y. A Hole-Conductor-Free, Fully Printable Mesoscopic Perovskite Solar Cell with High Stability. *Science* **2014**, *345*, 295-298.

(11) Rong, Y.; Hou, X.; Hu, Y.; Mei, A.; Liu, L.; Wang, P.; Han, H. Synergy of Ammonium Chloride and Moisture on Perovskite Crystallization for Efficient Printable Mesoscopic Solar Cells. *Nat. Commun.* **2017**, *8*, No. 14555.

(12) Liu, S.; Huang, W.; Liao, P.; Pootrakulchote, N.; Li, H.; Lu, J.; Li, J.; Huang, F.; Shai, X.; Zhao, X. 17% Efficient Printable Mesoscopic PIN Metal Oxide Framework Perovskite Solar Cells Using Cesium-Containing Triple Cation Perovskite. *J. Mater. Chem. A* **2017**, *5*, 22952-22958.

(13) Tress, W.; Marinova, N.; Moehl, T.; Zakeeruddin, S. M.; Nazeeruddin, M. K.; Grätzel, M. Understanding the Rate-Dependent J-V Hysteresis, Slow Time Component, and Aging in $CH_3NH_3PbI_3$ Perovskite Solar Cells: The Role of a Compensated Electric Field. *Energy Environ. Sci.* **2015**, *8*, 995-1004.

(14) Beilsten-Edmands, J.; Eperon, G.; Johnson, R.; Snaith, H.; Radaelli, P. Non-Ferroelectric Nature of the Conductance Hysteresis in $CH_3NH_3PbI_3$ Perovskite-Based Photovoltaic Devices. *Appl. Phys. Lett.* **2015**, *106*, No. 173502.

(15) Pham, N. D.; Zhang, C.; Tiong, V. T.; Zhang, S.; Will, G.; Bou, A.; Bisquert, J.; Shaw, P. E.; Du, A.; Wilson, G. J. Tailoring Crystal Structure of $FA_{0.83}Cs_{0.17}PbI_3$ Perovskite Through Guanidinium Doping for Enhanced Performance and Tunable Hysteresis of Planar Perovskite Solar Cells. *Adv. Funct. Mater.* **2019**, *29*, No. 1806479.

(16) Tiong, V. T.; Pham, N. D.; Wang, T.; Zhu, T.; Zhao, X.; Zhang, Y.; Shen, Q.; Bell, J.; Hu, L.; Dai, S.; Wang, H. Octadecylamine-Functionalized Single-Walled Carbon Nanotubes for Facilitating the Formation of a Monolithic Perovskite Layer and Stable Solar Cells. *Adv. Funct. Mater.* **2018**, *28*, No. 1705545.

(17) Rong, Y.; Hu, Y.; Ravishankar, S.; Liu, H.; Hou, X.; Sheng, Y.; Mei, A.; Wang, Q.; Li, D.; Xu, M. Tunable Hysteresis Effect for Perovskite Solar Cells. *Energy Environ. Sci.* **2017**, *10*, 2383-2391.

(18) Zimmermann, I.; Gratia, P.; Martineau, D.; Grancini, G.; Audinot, J. N.; Wirtz, T.; Nazeeruddin, M. K. Improved Efficiency and Reduced Hysteresis in Ultra-Stable Fully-Printable Mesoscopic

Perovskite Solar Cells Through Incorporation of CuSCN in the Perovskite Layer. *J. Mater. Chem. A* **2019**, *7*, 8073-8077.
(19) Adjokatse, S.; Fang, H.-H.; Loi, M. A. Broadly Tunable Metal Halide Perovskites for Solid-State Light-Emission Applications. *Mater. Today* **2017**, *20*, 413-424.
(20) Lu, J.; Lin, X.; Jiao, X.; Gengenbach, T.; Scully, A. D.; Jiang, L.; Tan, B.; Sun, J.; Li, B.; Pai, N. Interfacial Benzenethiol Modification Facilitates Charge Transfer and Improves Stability of cm-Sized Metal Halide Perovskite Solar Cells with up to 20% Efficiency. *Energy Environ. Sci.* **2018**, *11*, 1880-1889.
(21) Zhang, W.; Song, J.; Wang, D.; Deng, K.; Wu, J.; Zhang, L. Dual Interfacial Modification Engineering with p-Type NiO Nanocrystals for Preparing Efficient Planar Perovskite Solar Cells. *J. Mater. Chem. C* **2018**, *6*, 13034-13042.
(22) Xiao, J.-W.; Ma, S.; Yu, S.; Zhou, C.; Liu, P.; Chen, Y.; Zhou, H.; Li, Y.; Chen, Q. Ligand Engineering on CdTe Quantum Dots in Perovskite Solar Cells for Suppressed Hysteresis. *Nano energy* **2018**, *46*, 45-53.
(23) Pattanasattayavong, P.; Yaacobi-Gross, N.; Zhao, K.; Ndjawa, G. O. N.; Li, J.; Yan, F.; O'Regan, B. C.; Amassian, A.; Anthopoulos, T. D. Hole-Transporting Transistors and Circuits Based on the Transparent Inorganic Semiconductor Copper (I) Thiocyanate (CuSCN) Processed from Solution at Room Temperature. *Adv. Mater.* **2013**, *25*, 1504-1509.
(24) Yang, Y.; Pham, N. D.; Yao, D.; Zhu, H.; Yarlagadda, P.; Wang, H. Inorganic p-Type Semiconductors and Carbon Materials Based Hole Transport Materials for Perovskite Solar Cells. *Chin. Chem. Lett.* **2018**, *29*, 1242-1250.
(25) Arora, N.; Dar, M. I.; Hinderhofer, A.; Pellet, N.; Schreiber, F.; Zakeeruddin, S. M.; Grätzel, M. Perovskite Solar Cells with CuSCN Hole Extraction Layers Yield Stabilized Efficiencies Greater Than 20%. *Science* **2017**, *358*, 768-771.
(26) Bu, T.; Liu, X.; Zhou, Y.; Yi, J.; Huang, X.; Luo, L.; Xiao, J.; Ku, Z.; Peng, Y.; Huang, F. A Novel Quadruple-Cation Absorber for Universal Hysteresis Elimination for High Efficiency and Stable Perovskite Solar Cells. *Energy Environ. Sci.* **2017**, *10*, 2509-2515.
(27) Yao, D.; Zhang, C.; Pham, N. D.; Zhang, Y.; Tiong, V. T.; Du, A.; Shen, Q.; Wilson, G. J.; Wang, H. Hindered Formation of Photoinactive δ-$FAPbI_3$ Phase and Hysteresis-Free Mixed-Cation Planar Heterojunction Perovskite Solar Cells with Enhanced Efficiency via Potassium Incorporation. *J. Phys. Chem. Lett.* **2018**, *9*, 2113-2120.
(28) Perera, V.; Senevirathna, M.; Pitigala, P.; Tennakone, K. Doping CuSCN Films for Enhancement of Conductivity: Application in Dye-Sensitized Solid-State Solar Cells. *Sol. Energy Mater. Sol. Cells* **2005**, *86*, 443-450.
(29) Wang, H.; Guerrero, A.; Bou, A.; Al-Mayouf, A. M.; Bisquert, J. Kinetic and material properties of interfaces governing slow response and long timescale phenomena in perovskite solar cells. *Energy Environ. Sci*. **2019**, DOI: 10.1039/c9ee00802k
(30) Yokoyama, T.; Cao, D. H.; Stoumpos, C. C.; Song, T.-B.; Sato, Y.; Aramaki, S.; Kanatzidis, M. G. Overcoming Short-Circuit in Lead-Free $CH_3NH_3SnI_3$ Perovskite Solar Cells via Kinetically Controlled Gas–Solid Reaction Film Fabrication Process. *J. Phys. Chem. Lett.* **2016**, *7*, 776-782.
(31) Stranks, S. D.; Eperon, G. E.; Grancini, G.; Menelaou, C.; Alcocer, M. J.; Leijtens, T.; Herz, L. M.; Petrozza, A.; Snaith, H. J. Electron-Hole Diffusion Lengths Exceeding 1 Micrometer in an Organometal Trihalide Perovskite Absorber. *Science* **2013**, *342*, 341-344.
(32) Zaban, A.; Greenshtein, M.; Bisquert, J. Determination of the Electron Lifetime in Nanocrystalline Dye Solar Cells by Open-Circuit Voltage Decay Measurements. *ChemPhysChem* **2003**, *4*, 859-864.
(33) Wang, Q. Fast Voltage Decay in Perovskite Solar Cells Caused by Depolarization of Perovskite Layer. *J. Phys. Chem. C* **2018**, *122*, 4822-4827.
(34) Peng, J.; Wu, Y.; Ye, W.; Jacobs, D. A.; Shen, H.; Fu, X.; Wan, Y.; Wu, N.; Barugkin, C.; Nguyen, H. T. Interface Passivation Using Ultrathin Polymer-Fullerene Films for High-Efficiency Perovskite Solar Cells with Negligible Hysteresis. *Energy Environ. Sci.* **2017**, *10*, 1792-1800.
(35) Guerrero, A.; Garcia-Belmonte, G.; Mora-Sero, I.; Bisquert, J.; Kang, Y. S.; Jacobsson, T. J.; Correa-Baena, J.-P.; Hagfeldt, A. Properties of Contact and Bulk Impedances in Hybrid Lead Halide Perovskite Solar Cells Including Inductive Loop Elements. *J. Phys. Chem. C* **2016**, *120*, 8023-8032.

(36) Zarazua, I.; Han, G.; Boix, P. P.; Mhaisalkar, S.; Fabregat-Santiago, F.; Mora-Seró, I.; Bisquert, J.; Garcia-Belmonte, G. Surface Recombination and Collection Efficiency in Perovskite Solar Cells from Impedance Analysis. *J. Phys. Chem. Lett.* **2016**, *7*, 5105-5113.
(37) Pham, N. D.; Tiong, V. T.; Yao, D.; Martens, W.; Guerrero, A.; Bisquert, J.; Wang, H. Guanidinium Thiocyanate Selective Ostwald Ripening Induced Large Grain for High Performance Perovskite Solar Cells. *Nano Energy* **2017**, *41*, 476-487.
(38) Correa-Baena, J.-P.; Turren-Cruz, S.-H.; Tress, W.; Hagfeldt, A.; Aranda, C.; Shooshtari, L.; Bisquert, J.; Guerrero, A. Changes from Bulk to Surface Recombination Mechanisms between Pristine and Cycled Perovskite Solar Cells. *ACS Energy Lett.* **2017**, *2*, 681-688.
(39) Carrillo, J.; Guerrero, A.; Rahimnejad, S.; Almora, O.; Zarazua, I.; Mas-Marza, E.; Bisquert, J.; Garcia-Belmonte, G. Ionic Reactivity at Contacts and Aging of Methylammonium Lead Triiodide Perovskite Solar Cells. *Adv. Energy Mater.* **2016**, *6*, No. 1502246.
(40) Belisle, R. A.; Nguyen, W. H.; Bowring, A. R.; Calado, P.; Li, X.; Irvine, S. J.; McGehee, M. D.; Barnes, P. R.; O'Regan, B. C. Interpretation of Inverted Photocurrent Transients in Organic Lead Halide Perovskite Solar Cells: Proof of the Field Screening by Mobile Ions and Determination of the Space Charge Layer Widths. *Energy Environ. Sci.* **2017**, *10*, 192-204.
(41) Erdenebileg, E.; Scholz, L. E.; Hofacker, A.; Koerner, C.; Leo, K. Very Small Inverted Hysteresis in Vacuum-Deposited Mixed Organic-Inorganic Hybrid Perovskite Solar Cells. *Energy Technol.* **2017**, *5*, 1606-1611.
(42) Lopez-Varo, P.; Jiménez-Tejada, J. A.; García-Rosell, M.; Ravishankar, S.; Garcia-Belmonte, G.; Bisquert, J.; Almora, O. Device Physics of Hybrid Perovskite Solar Cells: Theory and Experiment. *Adv. Energy Mater.* **2018**, *8*, No. 1702772.
(43) Ravishankar, S.; Gharibzadeh, S.; Roldán-Carmona, C.; Grancini, G.; Lee, Y.; Ralaiarisoa, M.; Asiri, A. M.; Koch, N.; Bisquert, J.; Nazeeruddin, M. K. Influence of Charge Transport Layers on Open-Circuit Voltage and Hysteresis in Perovskite Solar Cells. *Joule* **2018**, *2*, 788-798.
(44) Almora, O.; Zarazua, I.; Mas-Marza, E.; Mora-Sero, I.; Bisquert, J.; Garcia-Belmonte, G. Capacitive Dark Currents, Hysteresis, and Electrode Polarization in Lead Halide Perovskite Solar Cells. *J. Phys. Chem. Lett.* **2015**, *6*, 1645-1652.
(45) Guerrero, A.; Bou, A.; Matt, G.; Almora, O.; Heumüller, T.; Garcia-Belmonte, G.; Bisquert, J.; Hou, Y.; Brabec, C. Switching Off Hysteresis in Perovskite Solar Cells by Fine-Tuning Energy Levels of Extraction Layers. *Adv. Energy Mater.* **2018**, *8*, No. 1703376.
(46) Dong, Q.; Fang, Y.; Shao, Y.; Mulligan, P.; Qiu, J.; Cao, L.; Huang, J. Electron-Hole Diffusion Lengths> 175 μm in Solution Grown $CH_3NH_3PbI_3$ Single Crystals. *Science* **2015**, *347*, 967-970.
(47) Fan, J.; Ma, Y.; Zhang, C.; Liu, C.; Li, W.; Schropp, R. E.; Mai, Y. Thermodynamically Self-Healing 1D-3D Hybrid Perovskite Solar Cells. *Adv. Energy Mater.* **2018**, *8*, No. 1703421.
(48) Cai, F.; Yan, Y.; Yao, J.; Wang, P.; Wang, H.; Gurney, R. S.; Liu, D.; Wang, T. Ionic Additive Engineering Toward High-Efficiency Perovskite Solar Cells with Reduced Grain Boundaries and Trap Density. *Adv. Funct. Mater.* **2018**, *28*, No. 1801985.
(49) Lin, Q.; Armin, A.; Nagiri, R. C. R.; Burn, P. L.; Meredith, P. Electro-Optics of Perovskite Solar Cells. *Nat. Photonics* **2015**, *9*, 106-112.
(50) Saliba, M. Perovskite Solar Cells Must Come of Age. *Science* **2018,** *359*, 388-389.
(51) Aristidou, N.; Sanchez-Molina, I.; Chotchuangchutchaval, T.; Brown, M.; Martinez, L.; Rath, T.; Haque, S. A. The Role of Oxygen in the Degradation of Methylammonium Lead Trihalide Perovskite Photoactive Layers. *Angew. Chem.* **2015**, *127*, 8326-8330.
(52) Roose, B.; Ummadisingu, A.; Correa-Baena, J.-P.; Saliba, M.; Hagfeldt, A.; Graetzel, M.; Steiner, U.; Abate, A. Spontaneous Crystal Coalescence Enables Highly Efficient Perovskite Solar Cells. *Nano Energy* **2017**, *39*, 24-29.
(53) Lam, C.; Wu, R.; Li, D.; Hair, M.; Neumann, A. Study of the Advancing and Receding Contact Angles: Liquid Sorption as a Cause of Contact Angle Hysteresis. *Adv. Colloid Interface Sci.* **2002**, *96*, 169-191.
(54) Yang, S.; Wang, Y.; Liu, P.; Cheng, Y.-B.; Zhao, H. J.; Yang, H. G. Functionalization of Perovskite Thin Films with Moisture-Tolerant Molecules. *Nature Energy* **2016,** *1*, No. 15016.

Graphical abstract